bioRxiv preprint doi: https://doi.org/10.1101/2024.04.02.587663; this version posted April 2, 2024. The copyright holder for this preprint (which was not certified by peer review) is the author/funder, who has granted bioRxiv a license to display the preprint in perpetuity. It is made available under aCC-BY 4.0 International license.

Single-cell analysis of lung epithelial cells reveals age and cell population-specific responses to SARS-CoV-2 infection in ciliated cells

Running Head: Single-cell analysis of SARS-CoV-2 in *H. Sapiens*

Raven M. Osborn[a,b,c], Christopher S. Anderson[d], Justin R. Leach[c], ChinYi Chu[e], Stephen Dewhurst[c], Thomas J. Mariani[f,g,h], Juilee Thakar#[a,b,c,g,i]

[a]Translational Biomedical Sciences Program, University of Rochester School of Medicine and Dentistry, Rochester, New York, USA

[b]Clinical and Translational Sciences Institute, University of Rochester School of Medicine and Dentistry, Rochester, New York, USA

[c]Department of Microbiology and Immunology, University of Rochester School of Medicine and Dentistry, Rochester, New York, USA

[d]Department of Medicine, Division of Infectious Diseases, University of Rochester School of Medicine and Dentistry, Rochester, New York, USA

[e]Department of Pediatrics, Center for Pediatric Biomedical Research, University of Rochester School of Medicine and Dentistry, Rochester, New York, USA

[f]Department of Pediatrics, Division of Neonatology, University of Rochester School of Medicine and Dentistry, Rochester, New York, USA

[g]Department of Biomedical Genetics, University of Rochester School of Medicine and Dentistry, Rochester, New York, USA

[h]Department of Environmental Medicine, University of Rochester School of Medicine and Dentistry, Rochester, New York, USA

[i]Department of Biostatistics and Computational Biology, University of Rochester School of Medicine and Dentistry, Rochester, New York, USA

#Address correspondence to Juilee Thakar, Juilee_Thakar@URMC.Rochester.edu

Abstract word count: 248
Text word count: 4988

bioRxiv preprint doi: https://doi.org/10.1101/2024.04.02.587663; this version posted April 2, 2024. The copyright holder for this preprint (which was not certified by peer review) is the author/funder, who has granted bioRxiv a license to display the preprint in perpetuity. It is made available under aCC-BY 4.0 International license.

Abstract

The ability of SARS-CoV-2 to evade antiviral immune signaling in the airway contributes to the severity of COVID-19 disease. Additionally, COVID-19 is influenced by age and has more severe presentations in older individuals. This raises questions about innate immune signaling as a function of lung development and age. Therefore, we investigated the transcriptome of different cell populations of the airway epithelium using pediatric and adult lung tissue samples from the LungMAP Human Tissue Core Biorepository. Specifically, lung lobes were digested and cultured into a biomimetic model of the airway epithelium on an air-liquid interface. Cells were then infected with SARS-CoV-2 and subjected to single-cell RNA sequencing. Transcriptional profiling and differential expression analysis were carried out using Seurat.

The clustering analysis identified several cell populations: club cells, proliferating epithelial cells, multiciliated precursor cells, ionocytes, and two biologically distinct clusters of ciliated cells ($FOXJ1^{high}$ and $FOXJ1^{low}$). Interestingly, the two ciliated cell clusters showed different infection rates and enrichment of processes involved in ciliary biogenesis and function; we observed a cell-type-specific suppression of innate immunity in infected cells from the $FOXJ1^{low}$ subset. We also identified a significant number of genes that were differentially expressed in lung cells derived from children as compared to adults, suggesting the differential pathogenesis of SARS-CoV-2 infection in children versus adults. We discuss how this work can be used to identify drug targets to modulate molecular signaling cascades that mediate an innate immune response and begin to understand differences in COVID-19 outcomes for pediatric vs. adult populations.

bioRxiv preprint doi: https://doi.org/10.1101/2024.04.02.587663; this version posted April 2, 2024. The copyright holder for this preprint (which was not certified by peer review) is the author/funder, who has granted bioRxiv a license to display the preprint in perpetuity. It is made available under aCC-BY 4.0 International license.

Importance

Viral innate immune evasion leads to uncontrolled viral spread in infected tissues and increased pathogenicity in COVID-19. Understanding the dynamic of the antiviral signaling in lung tissues may help us to understand which molecular signals lead to more severe disease in different populations, particularly considering the enhanced vulnerability of older populations. This study provides foundational insight into the age-related differences in innate immune responses to SARS-CoV-2, identifying distinct patterns of infection and molecular signaling in different cell populations of airway epithelial cells from pediatric and adult lung tissues. The findings provide a deeper understanding of age-related differences in COVID-19 pathology and pave the way for developing targeted therapies.

Introduction

SARS-CoV-2, the virus responsible for the COVID-19 pandemic, is a positive-sense, single-stranded RNA virus that belongs to the coronaviridae family. SARS-CoV-2 binds host receptors for entry, and once inside the cell, the virus hijacks the host cell's machinery to replicate its genome and produce viral proteins. Newly synthesized viral proteins and genomes assemble to create virions, which are then released from the cell where they can infect neighboring cells (1). During this process, host cell mechanisms for detecting the virus are in a race to prevent it from spreading to other cells. Viral infection induces secretion of type I and type III interferon, which leads to the induction of antiviral genes in the neighboring cells, making them resistant to viral infection through paracrine signaling (2-4). The balance between interferon secretion and viral spread determines the state of the innate immune response (2, 4).

bioRxiv preprint doi: https://doi.org/10.1101/2024.04.02.587663; this version posted April 2, 2024. The copyright holder for this preprint (which was not certified by peer review) is the author/funder, who has granted bioRxiv a license to display the preprint in perpetuity. It is made available under aCC-BY 4.0 International license.

A primary method for preventing the uncontrolled spread of SARS-CoV-2 after an organism has been infected is the robust induction of innate antiviral signaling cascades. Similar to other respiratory RNA viruses like Influenza, SARS-CoV-2 suppresses the antiviral host response. However, it has been demonstrated that SARS-CoV-2 can suppress the host's antiviral response to a much greater extent than influenza in animal models (5). Furthermore, the antiviral interferon response has been inversely correlated with COVID-19 pathology (3, 6, 7).

Unsurprisingly, the inverse correlation between interferon secretion and severe coronavirus-related pathology is exacerbated in older age groups (7). In COVID-19, children generally experience milder acute illness; however, post-acute sequelae and Multisystem Inflammatory Syndrome in Children (MIS-C) occur in 1 of approximately 3,000 to 4,000 pediatric cases (8-10). One of the objectives of the present study was, therefore, to compare innate immune responses to SARS-CoV-2 in cells from children versus adults, with the goal of identifying and understanding age-related differences in these signaling pathways.

Interferon is the chief regulator of antiviral paracrine signaling, a mechanism by which cells adjacent to virus-infected cells can be driven into an antiviral state, thereby reducing viral spread. Many studies have interrogated this subject using cell lines, which don’t originate from the lung, or require the transduction of a known SARS-CoV-2 entry factor to support viral infection (5, 11, 12). Here, we have examined how these antiviral pathways are regulated after SARS-CoV-2 infection in primary human lung epithelial cells, using a biomimetic model cultured on an air-liquid interface that preserves the pseudostratification and differentiated functions of the normal lung epithelium.

SARS-CoV-2 infection is predominantly initiated and spread through cells in the airway epithelium. The respiratory epithelium comprises many different cell types, and SARS-CoV-2

bioRxiv preprint doi: https://doi.org/10.1101/2024.04.02.587663; this version posted April 2, 2024. The copyright holder for this preprint (which was not certified by peer review) is the author/funder, who has granted bioRxiv a license to display the preprint in perpetuity. It is made available under aCC-BY 4.0 International license.

virions infect those cells as they move throughout the respiratory system (13). Interestingly, the most commonly cited host entry factors for SARS-CoV-2 have heterogenous expression on cell-types along the respiratory system and within the cells of the same type (14). Mild and asymptomatic infections are typically restricted to ciliated and goblet cells in the nasal passages or upper respiratory tract (14), while more severe illnesses and pathology occur when the virus travels down to the parenchyma, infecting and injuring type II alveolar cells, disrupting the epithelial layer and reducing gas exchange – resulting in shortness of breath and respiratory distress (1). Therefore, investigating the host response to SARS-CoV-2 in cells of the conducting airway is important in understanding and preventing severe COVID-19 pathology. Due to the heterogeneity of cell types in the lung epithelium, we utilized single-cell RNA sequencing to discern cell-type-specific host responses in cultured primary lung epithelial cells.

Materials and Methods

Ethics statement

Donor lungs were provided through the federal United Network of Organ Sharing via the National Disease Research Interchange and the International Institute for Advancement of Medicine. With written consent, dissociated lung cells from deceased donors were entered into the LungMAP program's biorepository and were utilized in this study. The University of Rochester's Institutional Review Board approved and oversaw this study (RSRB00047606).

Primary human cells

bioRxiv preprint doi: https://doi.org/10.1101/2024.04.02.587663; this version posted April 2, 2024. The copyright holder for this preprint (which was not certified by peer review) is the author/funder, who has granted bioRxiv a license to display the preprint in perpetuity. It is made available under aCC-BY 4.0 International license.

The LungMAP program's biorepository was utilized in this study. The University of Rochester's Institutional Review Board approved and oversaw this study (RSRB00047606). The study cohort included five infants (under six months old) and two adult donors (over fifty years old). All donors were male, two had an unknown race, and five were white. Pathologist notes from all donors showed normal lung structure; all pediatric donors had normal lung development, and both adult donors had some signs of chronic inflammation. None of the pathologist notes indicated a lung-associated cause of death.

Viruses

The following reagents were deposited by the Centers for Disease Control and Prevention and obtained through BEI Resources, NIAID, NIH: SARS-Related Coronavirus 2, Isolate Hong Kong/VM20001061/2020, NR-52282. SARS-CoV-2 was propagated and titered using African green monkey kidney epithelial Vero E6 cells (American Type Culture Collection, CRL-1586) in Eagle's Minimum Essential Medium (Lonza, 12-125Q) supplemented with 2% fetal bovine serum (FBS) (Atlanta Biologicals), 2 mM l-glutamine (Lonza, BE17-605E), and 1% penicillin (100 U/ml) and streptomycin (100 ug/ml). Virus stocks were stored at − 80°C. All work involving infectious SARS-CoV-2 was performed in the Biosafety Level 3 (BSL-3) core facility of the University of Rochester, with institutional biosafety committee (IBC) oversight.

Cell culture on air-liquid interface

Primary human lung cells were cultured on an air-liquid interface as described (15, 16). Briefly, lung tissue issues were digested with a protease cocktail, and adherent cells were expanded with bronchial epithelial cell growth medium (Lonza, CC-3170) and then transferred

bioRxiv preprint doi: https://doi.org/10.1101/2024.04.02.587663; this version posted April 2, 2024. The copyright holder for this preprint (which was not certified by peer review) is the author/funder, who has granted bioRxiv a license to display the preprint in perpetuity. It is made available under aCC-BY 4.0 International license.

153 to a collagen-coated transwell plate (Corning, 3470) until each well reached a transepithelial
154 electrical resistance (TEER) measurement of >300 ohms. Cells were then placed on an air-liquid
155 interface (ALI) by removing media from the apical layer of the transwell chamber and
156 continuing to feed cells on the basolateral layer as they differentiate. Cells were differentiated for
157 4-5 weeks at ALI before experiment use.
158

159 SARS-CoV-2 infections of airway epithelial cells

160 The apical layer of primary lung cells cultured at the air-liquid interface for 4-5 weeks
161 was inoculated with SARS-CoV-2 (BEI, NR-52281, hCoV-19/USA-WA1/2020) at an MOI of 5
162 (titered in VeroE6 cells) in phosphate-buffered saline containing calcium and magnesium
163 (PBS++; Gibco, 14040-133) and incubated at 37°C for 1.5 hours. Next, the infectious solution
164 was removed, and the apical layer was washed with PBS++ (PBS with added calcium and
165 magnesium). Cells were then incubated for 48 hours.
166

167 SARS-CoV-2 inactivation and scRNA-seq sample preparation

168 Primary human lung cells infected with SARS-CoV-2 were prepared for scRNA-seq
169 using a method described by this group (17, 18). Briefly, cultured cells were washed by
170 dispensing and aspirating 37°C HEPES buffered saline solution (Lonza, CC-5022) and then
171 dissociated with 0.025% Trypsin/EDTA (Lonza, CC-5012) for 10 min at 37°C. Dissociated cells
172 were aspirated using a wide-bore pipette tip and placed in a tube containing ice-cold Trypsin
173 Neutralization Solution (Lonza, CC-5002); this was repeated to maximize cell collection. Cells
174 were then pelleted by centrifugation (300 x *g* for 5 min), resuspended in chilled HEPES, and

bioRxiv preprint doi: https://doi.org/10.1101/2024.04.02.587663; this version posted April 2, 2024. The copyright holder for this preprint (which was not certified by peer review) is the author/funder, who has granted bioRxiv a license to display the preprint in perpetuity. It is made available under aCC-BY 4.0 International license.

centrifugally pelleted again. Next, the supernatant was removed using a wide-bore pipette tip, and the cell pellet was resuspended in 100 µl of chilled 1X DPBS. Next, 1 ml of a chilled 1:1 methanol acetone mixture was added to the cells dropwise with continuous gentle agitation. Cells were incubated on ice for 1 hour, washed in PBS++, counted, and finally resuspended in a cold SSC cocktail (3× Lonza AccuGENE SSC, BMA51205 + 0.04% BSA + 1mM DTT + 0.2 U/ µl RNase1 inhibitor).

Library preparation and sequence mapping

Following SARS-CoV-2 inactivation and rehydration, cell suspensions were processed to generate single-cell RNA-Seq libraries using Chromium Next GEM Single Cell 3′ GEM, Library and Gel Bead Kit v3.1 (10x Genomics), per the manufacturer's recommendations, as summarized below. To minimize the addition of the rehydration buffer, a maximum of 4 µl cell suspension was used in the GEM (Gel Bead-in-Emulsion) generation step. Subsequently, samples were loaded on a Chromium Single-Cell Instrument (10x Genomics, Pleasanton, CA, USA) to generate single-cell GEMs. GEM reverse transcription (GEM-RT) was performed to produce a barcoded, full-length cDNA from poly-adenylated mRNA. After incubation, GEMs were broken, the pooled GEM-RT reaction mixtures were recovered, and cDNA was purified with silane magnetic beads (DynaBeads MyOne Silane Beads, PN37002D, ThermoFisher Scientific). PCR further amplified the purified cDNA to generate sufficient material for library construction. Enzymatic fragmentation and size selection was used to optimize the cDNA amplicon size, and indexed sequencing libraries were constructed by end repair, A-tailing, adaptor ligation, and PCR. The final libraries contain the P5 and P7 priming sites used in Illumina bridge amplification. Sequence data were generated using Illumina's NovaSeq 6000.

bioRxiv preprint doi: https://doi.org/10.1101/2024.04.02.587663; this version posted April 2, 2024. The copyright holder for this preprint (which was not certified by peer review) is the author/funder, who has granted bioRxiv a license to display the preprint in perpetuity. It is made available under aCC-BY 4.0 International license.

Samples were demultiplexed and counted using 10x Cell Ranger version 6.0.1 with standard parameters. Samples were aligned against a combined reference containing the 10x provided human reference (GRCh38-2020-A) and NCBI GenBank SARS-CoV-2 reference sequence MT644268.

Quality control and cell clustering

Analysis of scRNA-seq data was done using the Seurat v.4 R package (19). Cells expressing greater than 6000 genes or over 10% mitochondrial genes were omitted from the analysis. Sample integration was performed using the recommended scRNA-seq integration pipeline with canonical correlation analysis (CCA). Linear dimension reduction using principal component analysis (PCA) was then performed on the integrated data to determine the appropriate number of dimensions for Seurat's clustering algorithm.

Cell cluster annotation

Cell clusters were annotated using the Seurat v.4 R package (19). For each cluster, we performed the Wilcoxon Rank Sum test with a log fold change threshold of at least 0.25. Differentially expressed genes (DEGs) that are specific to each cluster were used for enrichment analysis with ToppGene Suite's ToppCell Atlas to determine the cell type of each cluster (20). Functional analysis of DEGs was performed with the clusterProfiler 4.2 R package alongside Gene Ontology terms for biological processes (21). Cluster annotations were further performed for each cell using gene set enrichment analysis against a database of known cell type markers

bioRxiv preprint doi: https://doi.org/10.1101/2024.04.02.587663; this version posted April 2, 2024. The copyright holder for this preprint (which was not certified by peer review) is the author/funder, who has granted bioRxiv a license to display the preprint in perpetuity. It is made available under aCC-BY 4.0 International license.

with the scType R package (22). Finally, cell assignment proportions were compared using the Chi-square test and visualized using the dittoSeq R package version 1.8.1 (23).

Trajectory and pseudotime analysis

Normalized gene expression data, cluster assignments, UMAP embeddings, and partitions were converted from Seurat objects to a monocle object for trajectory and pseudotime analysis using the Monocle3 R package version 1.3.1 (24). Trajectory analysis was performed with the Seurat-assigned clusters on the entire dataset by assigning all cells to the same partition in Monocle3. Pseudotime was calculated using the basal cells as the root cluster when ordering cells. Pseudotime comparisons were performed with the Wilcoxon Rank Sum test with a Benjamini-Hochberg corrected adjusted p-value of less than .05.

Cell-cell communication analysis

Cell-cell communication analysis was performed using the Liana framework from the Liana R package version 0.1.12 (25). A Robust Rank Aggregate score was calculated using algorithms from the following methods: NATMI, iTalk (logFC Mean), Connectome, SingleCellSignalR, and CellphoneDB (26-31). Context deconvolution was performed using the standard Liana framework in conjunction with Tensor-cell2cell and SingleCellSignalR (28, 32). Finally, footprint enrichment analysis with ligand-receptor pairs was performed using genesets

bioRxiv preprint doi: https://doi.org/10.1101/2024.04.02.587663; this version posted April 2, 2024. The copyright holder for this preprint (which was not certified by peer review) is the author/funder, who has granted bioRxiv a license to display the preprint in perpetuity. It is made available under aCC-BY 4.0 International license.

from PROGENy and decoupleR R packages as recommended from the Liana context factorization pipeline (33, 34).

Age and infection differential expression analysis

Differential gene expression analyses for age and infection were conducted using the MAST method in the FindMarkers function in the Seurat R package. The differentially expressed genes had log fold change >= 0.2 and a Benjamini-Hochberg corrected p-values <.05 (35). Differential pathway analysis was performed using the FindMarkers function using the MAST R package (version 1.22.0) with a Benjamini-Hochberg corrected p-value threshold of less than .001 for the mock vs. infected contrast and .0001 for the age contrast (35). Cluster-specific intersections were visualized using the UpSetR (version 1.4.0) and ComplexUpset (version 1.3.3) R packages (36, 37).

Gene functional annotation

Enrichment of DEGs from each cluster was performed and visualized using the clusterProfiler 4.2 R package (21). Over-representation analysis with clusterProfiler was used with genesets from the Kyoto Encyclopedia of Genes and Genomes (KEGG) 2021 pathway database with disease-associated pathway manually omitted (38). Gene set enrichment analysis was performed using the AUCell R Package version 1.18.1. AUCell scores were calculated using the top 10% of ranked genes in each cell against the KEGG genesets, a manually curated list of

bioRxiv preprint doi: https://doi.org/10.1101/2024.04.02.587663; this version posted April 2, 2024. The copyright holder for this preprint (which was not certified by peer review) is the author/funder, who has granted bioRxiv a license to display the preprint in perpetuity. It is made available under aCC-BY 4.0 International license.

antiviral genes, and a geneset from a published overexpression screen of interferon-stimulated genes (39, 40). Cluster-specific intersections were visualized using the UpSetR (version 1.4.0) and ComplexUpset (version 1.3.3) R packages (36, 37).

Results

Primary lung epithelial cells cluster into six cell types, including two distinct ciliated cell clusters

Single-cell RNA sequencing (scRNA-seq) data from 52,482 cells from pediatric and adult donors with or without SARS-CoV-2 infection clustered into six cell populations (Fig. 1A) (Fig. 1A, SFig. 1). Annotation of these six cell populations using overrepresentation analysis (ORA) and gene set enrichment analysis (GSEA) revealed that primary human epithelial cells cultured on an air-liquid interface differentiated into FOXJ1^{low} ciliated cells, club cells, FOXJ1^{high} ciliated cells, basal cells, multiciliated precursor cells, and ionocytes (Fig. 1B-C). Functional enrichment analysis of cluster markers supported the underlying biological processes associated with those cell populations (Fig. 1D). Ciliated cell clusters had significant enrichment of pathways involved in cilium assembly, cilium organization, and microtubule-based movement (Fig. 1D). More transient cell populations (basal cells and multiciliated precursors) showed enrichment in pathways involving cell division (Fig. 1D). In total, our primary human epithelial cells cultured on an air-liquid interface differentiated into 35,279 (67.22%) FOXJ1^{low} ciliated cells, 9,194 (17.52%) club cells, 4,138 (7.89%) FOXJ1^{high} ciliated cells, 2,879 (5.49%) basal

bioRxiv preprint doi: https://doi.org/10.1101/2024.04.02.587663; this version posted April 2, 2024. The copyright holder for this preprint (which was not certified by peer review) is the author/funder, who has granted bioRxiv a license to display the preprint in perpetuity. It is made available under aCC-BY 4.0 International license.

cells, 725 (1.38%) multiciliated precursor cells, and 267 (.51%) ionocytes (Fig. 1E-F). These proportions of cell populations were similar across most donors (Fig. 1F).

We found that the proportion of cells in each cluster was the same in control samples as well as samples infected with SARS-CoV-2 (adjusted $p>0.05$)(Fig.1G)(SFig. 1A). Similarly, the proportions of cells in each population were not significantly different between pediatric and adult donors (Fig. 1H)(SFig. 1B). Further investigation of cell cycle scoring revealed that there were no significant differences in the proportion of cells in G1, G2M, or S phase between each donor, donor age, or treatment status (SFig. 2A-G). Although a high proportion of FOXJ1^{low} ciliated cells were found to have a G2M cell cycle score, this was due to low-level expression of a small subset of genes.

The lung epithelium primarily consists of fully differentiated cells, but injury can cause cells to dedifferentiate into their progenitors (41-43). We were interested to see if there were differences in cell differentiation among age cohorts or treatment status. Trajectory analysis of the main partition revealed that the differentiation trajectory of our cells began with the most "stem-like" cell type, basal cells, and continued onto club cells, multiciliated precursors, FOXJ1^{low} ciliated cells, and finally FOXJ1^{high} ciliated cells (Fig.2). Trajectories of all the cells from each sample showed no obvious differences in cell trajectories between any age or treatment status. Further, we found that the two ciliated cell types were related and did not arise from two different branches. Rather, FOXJ1^{high} ciliated cells arise from FOXJ1^{low} ciliated cells. Indeed, our pseudotime analysis revealed that FOXJ^{high} ciliated cells were the most terminally differentiated cell type, followed by FOXJ1^{low} ciliated cells, multiciliated precursors, club cells, ionocytes, and finally basal cells (which were defined as the root cells in our analysis) (42-44) (Fig. 2)(SFig. 3).

bioRxiv preprint doi: https://doi.org/10.1101/2024.04.02.587663; this version posted April 2, 2024. The copyright holder for this preprint (which was not certified by peer review) is the author/funder, who has granted bioRxiv a license to display the preprint in perpetuity. It is made available under aCC-BY 4.0 International license.

FOXJ1^{low} ciliated cells exhibit distinctly low ligand-receptor communication patterns

Intercellular communication is vital in preserving homeostasis and serves as one of the primary mechanisms for eliciting an immune response in complex biological systems such as the airway epithelium. To investigate intercellular communication in our primary cells, we aggregated cell-cell communication scores from several methods. Ionocytes had many inferred ligand-receptor interactions when top receptors are ordered by magnitude and then specificity; these interactions occur with ionocytes, suggesting regulatory feedback, or basal cells (Fig 3A).

When quantifying the frequency of inferred outgoing signals through ligand expression, basal cells had the highest frequency (2201), followed by club cells (1809), multiciliated precursors (1739), FOXJ1^{high} ciliated cells (1695), ionocytes (1601), and FOXJ1^{low} ciliated cells (339)(Fig. 3B)(Table 1). Basal cells were also found to have the highest frequency of inferred signal reception (2016) followed by ionocytes (1917), multiciliated precursors (1843), club cells (1815), FOXJ1^{high} ciliated cells (1698), and FOXJ1^{low} ciliated cells (95)(Fig. 3B)(Table 1)(SFig. 4). Interestingly, the most numerous cell population, FOXJ1^{low} ciliated cells, had very few inferred intrapopulation and interpopulation ligand-receptor interactions as a sender or receiver (Fig. 3B)(Table 1). However, FOXJ1^{low} ciliated cells were ~3.5 times more likely to send signals rather than receive them (Fig. 3B)(Table 1).

When comparing the top 25 most significant ligand-receptor pairs identified by all the cell-cell communication algorithms, we found 13 (34%) pairs common across age and infection comparisons. Additionally, there were few context-specific ligand-receptor pairs for each group;

bioRxiv preprint doi: https://doi.org/10.1101/2024.04.02.587663; this version posted April 2, 2024. The copyright holder for this preprint (which was not certified by peer review) is the author/funder, who has granted bioRxiv a license to display the preprint in perpetuity. It is made available under aCC-BY 4.0 International license.

one in mock samples (C3-GRM7), one in SARS-CoV-2-infected samples (PROS1-TYRO3), two in pediatric samples (GDF15-RET, VEGFB-RET), and six in adult samples (MMP1-CD44, TGFB1-CAV1, TGFB1-SDC2, TIMP3-CD44, DSC3-DSG3, SDC2-PTPRJ)(Fig. 3C).

To better understand the drivers behind these age or treatment-dependent differences, we performed cell-cell communication analysis on each sample to generate a tensor of ligand-receptor interactions and decomposed the tensor into communication patterns. The ionocyte cluster did not have enough representation in all samples, so we excluded ionocytes from samples with low counts in downstream analysis. After tensor deconvolution, we found ten significant factors that inform cell-cell communication patterns with distinct ligand-receptor pair expression patterns (Fig. 3D)(SFig. 5). Factor loadings were compared between treatment status and age. Surprisingly, we found no significant differences between treatment statuses. Still, factor 2 and factor 10 were significantly different between age groups (Fig. 3E)(Fig. 3F)(SFig. 6)(SFig. 7). Further exploration of the pathways associated with each factor revealed that factor 2 and 10 were downstream signaling typically involved in an antiviral response (Fig. 3G). Factor 2 was associated with increased NFκB activity and low MAPK, PI3K, and TRAIL signaling, while factor 10 was associated with reduced TRAIL signaling. These age-related differences in antiviral signaling prompted us to explore the differences in our age cohorts.

Age-related differences varied by cluster and infection status

Comparisons of cluster-specific gene-expression changes revealed several differences between adult and pediatric donors. Using only the cells from mock-infected samples, we found that the total number of DEGs and the number of unique DEGs varied between clusters; notably,

bioRxiv preprint doi: https://doi.org/10.1101/2024.04.02.587663; this version posted April 2, 2024. The copyright holder for this preprint (which was not certified by peer review) is the author/funder, who has granted bioRxiv a license to display the preprint in perpetuity. It is made available under aCC-BY 4.0 International license.

346 only a single gene was detected across all 6 cell types (RPS26), and only 22 genes were detected
347 when we excluded the smallest cluster, ionocytes, from this analysis (SFig. 7A). Similar to the
348 uninfected samples, we found that the total number of DEGs and the number of unique DEGs
349 varied between clusters. There were 81 genes that were unique to ciliated cell populations, while
350 basal and club cells had the highest combined number of DEGs in common. There were only
351 three genes (RPS26, AL627171.2, and SARS-CoV-2) differentially expressed between adult and
352 pediatric donors across all cell populations (SFig. 7B). Geneset enrichment analysis of combined
353 mock and infected data showed that age-related DEGs in ciliated cells were highly related to
354 ribosomal activity. In contrast, ciliated cells, basal cells, club cells, and multiciliated precursor
355 cells showed differences in the coronavirus disease and antigen processing and presentation
356 genesets (SFig. 8D)(SFig. 8E).

357 When comparing the age-related DEGs for each cluster in infected and mock samples, we
358 found some interesting functional differences. The majority of age-related DEGs in FOXJ1^{low}
359 ciliated cells were found in both mock and infected samples, while all other cell populations
360 showed a stronger age-related difference in mock samples (Fig. 4A, C, E, and G). In FOXJ1^{low}
361 ciliated cells, age-related DEGs had the strongest association in “Coronavirus disease” and
362 “Ribosome” pathways, which were enriched in both treatment conditions alongside the “Antigen
363 processing and presentation” pathway (Fig. 4B). Club cells, however, showed an age-related
364 enrichment in “Coronavirus disease” and “Antigen processing and presentation” in both
365 treatments, but “Ribosome” pathway enrichment was only found in the infected samples. On the
366 other hand, we observed an age-related enrichment in the “Ribosome” and “Coronavirus
367 disease” pathways in infected samples, while “Antigen processing and presentation” was

bioRxiv preprint doi: https://doi.org/10.1101/2024.04.02.587663; this version posted April 2, 2024. The copyright holder for this preprint (which was not certified by peer review) is the author/funder, who has granted bioRxiv a license to display the preprint in perpetuity. It is made available under aCC-BY 4.0 International license.

368 enriched in both treatments from FOXJ1^{high} ciliated cells. Conversely, basal cells had little
369 overlap in pathway enrichment between mock and infected samples (Fig. 4G, H)

370 Broadly, the large numbers of DEGs between adult and pediatric populations narrowed
371 in SARS-CoV-2-infected samples compared to mock samples (Fig. 4A, C, E, and G). Cluster-
372 specific functional analysis of age-associated DEGs in mock only, infected only, and in both
373 sample sets showed that many of the age-related DEGs in control samples were related to protein
374 synthesis, while age-related DEGs in infected samples were metabolism-related (Fig. 4B, D, F,
375 and H). In addition, the largest clusters (FOXJ1^{low} ciliated cells, club cells, and FOXJ1^{high}
376 ciliated cells) all had age-related differences in "Antigen Processing and Presentation" in mock
377 and infected samples. Perhaps the most striking finding to emerge from these analyses was that
378 the annotated transcript for SARS-CoV-2 was consistently higher in pediatric samples compared
379 to adult samples, with the highest difference between pediatric vs. adult samples being detected
380 in FOXJ1^{low} ciliated cells (a 3.120 log fold change).

381

382 FOXJ1^{low} ciliated cells are highly infected by SARS-CoV-2

383 Common SARS-CoV-2 entry factors ACE2, TMPRSS2, NRP1, AXL, FURIN, and
384 CTSL showed heterogeneous expression levels across cell populations. The commonly cited
385 entry factor, ACE2, had very low expression in all clusters. Interestingly, TMPRSS2 and CTSL
386 were the most commonly expressed entry factors, with around 10-30% of cells expressing them
387 in all clusters with the highest distribution and average expression level in FOXJ^{high} ciliated cells
388 (Fig. 5A). When comparing the expression level and percentage of cells expressing each gene by
389 infection status in each cluster, there were no significant differences in gene expression among

bioRxiv preprint doi: https://doi.org/10.1101/2024.04.02.587663; this version posted April 2, 2024. The copyright holder for this preprint (which was not certified by peer review) is the author/funder, who has granted bioRxiv a license to display the preprint in perpetuity. It is made available under aCC-BY 4.0 International license.

common SARS-CoV-2 entry factors ACE2, TMPRSS2, NRP1, AXL, FURIN, CTSL (SFig. 9A). Despite evidence of low expression of SARS-CoV-2 entry factors in cells from both mock and infected samples, FOXJ1^{low} ciliated cells had the highest overall expression of SARS-CoV-2 transcripts in qualitative and quantitative analysis (Fig. 5B)(Fig. 5C).

Comparisons of mock and infected samples resulted in the identification of cluster-specific infection-related DEGs. Similar to our age-related analysis, we found that the total number of DEGs and the number of unique DEGs varied between clusters; FOXJ1^{low} ciliated cells had 17 total and 6 unique genes (.35 distinct proportion), club cells had 170 total and 65 unique genes (.38 distinct proportion), FOXJ1^{high} ciliated cells showed 280 total and 175 unique genes (.63 distinct proportion), basal cells had 30 total and 11 unique genes (.37 distinct proportion), multiciliated precursor cells had 5 total and 0 unique genes, while ionocytes showed 2 total and 0 unique genes (Fig. 5D). We found only two genes that were differentially expressed between mock and infected samples across all cell populations; the transcript for SARS-CoV-2 and SCGB3A1, a gene that encodes a secreted protein involved in regulating epithelial cell proliferation, differentiation, morphogenesis, and defines secretory cell subsets (45, 46) (Fig. 5D). Strikingly, there were no ciliated-cell-specific DEGs between mock and infected samples. Moreover, ciliated cells only had 9 infection-related DEGs in common (Fig. 5E).

Investigation into the DEGs revealed that FOXJ1^{low} ciliated cells (the most susceptible to SARS-CoV-2 infection) had a muted antiviral response to SARS-CoV-2. In contrast, FOXJ1^{high} ciliated cells (which were less susceptible to the virus) had DEGs associated with a robust antiviral response (ISG15, MX1, and IFI27), dysregulated mucus secretion (MUC5B and BPIFB1), and down-regulated ciliogenesis (HYDIN) (Fig. 5F).

bioRxiv preprint doi: https://doi.org/10.1101/2024.04.02.587663; this version posted April 2, 2024. The copyright holder for this preprint (which was not certified by peer review) is the author/funder, who has granted bioRxiv a license to display the preprint in perpetuity. It is made available under aCC-BY 4.0 International license.

412 Stark differences in the host responses from each ciliated cell type prompted us to
413 perform differential functional analysis between the two ciliated cell types. Metabolic and
414 translation-relevant signaling pathways were significantly different between FOXJ1^{low} ciliated
415 cells and FOXJ1^{high} ciliated cells (Fig. 6A). However, FOXJ1^{high} ciliated cells had more
416 significant enrichment of pathways involved in ciliogenesis and cilia motility (Fig. 6B). These
417 differences in biological functions are typically indicated by cilium subtypes, which is evident in
418 the microanatomy of the cilium itself (Fig. 6C). FOXJ1^{high} ciliated cells had enrichment in
419 axoneme assembly, dynein binding, and microtubule motor movement, typical of 9+2 cilium
420 microanatomy (Fig. 6B). In contrast, FOXJ1^{low} ciliated cells were not enriched in the
421 compartments and showed a much lower level of canonical ciliated cell marker expression (Fig.
422 6B)(SFig. 10A) (SFig. 10B).
423

424 Cell-type-specific responses to SARS-CoV-2 infection

425 After finding many differences in the DEGs, we were interested in understanding how
426 cluster-specific DEGs contributed to functional responses. Functional enrichment of each
427 cluster's DEGs after infection showed a stark difference in enriched pathways (Fig. 7A). Despite
428 FOXJ1^{low} ciliated cells having the highest proportion of infected cells, all cell populations
429 showed significant enrichment of the "Coronavirus disease" pathway, with the lowest p-value in
430 club cells. Overall, FOXJ1^{high} ciliated cells had a response pattern more similar to club cells than
431 FOXJ1^{low} ciliated cells (Fig. 7A). When interrogating the expression of interferon-related
432 transcription factors and key genes, we found that all cell populations had low expression levels
433 of factors mediating an interferon response regardless of infection status. (Fig. 7B). Also, no

bioRxiv preprint doi: https://doi.org/10.1101/2024.04.02.587663; this version posted April 2, 2024. The copyright holder for this preprint (which was not certified by peer review) is the author/funder, who has granted bioRxiv a license to display the preprint in perpetuity. It is made available under aCC-BY 4.0 International license.

clusters significantly differed in type 1 or 3 interferon-related genes in infected samples compared to mock (Fig. 7C).

Further, we extended the pathway analysis by incorporating all expressed genes for each cell independently (see methods). The comparison of the cell-specific pathway activities found more differences across age than the infection status (Fig. 7D and E). The ciliated cell clusters, club cells, and basal cells had significantly different pathway activities across infection status, with club cells having the most (38 pathways); we detected only 6 common pathways between all clusters, including the "Coronavirus disease" pathway (Fig. 7D). Both ciliated populations and club cells had significant activity in "ISGs," a previously described list of over 200 interferon-stimulated genes (Fig. 7F)(39, 40). Pathway scoring at the single cell level revealed that FOXJ1^{low} and FOXJ1^{high} ciliated cells both had significant activity in the "Rig-I-like receptor signaling pathway" along with basal cells (Fig. 7A and F). Club cells and FOXJ1^{high} ciliated cells had significant activity in "Cytosolic DNA-sensing" and "JAK-STAT signaling" pathways, while FOXJ1^{high} ciliated cells were the only population to have activity in the "NOD-like receptor signaling pathway"(Fig. 7F). FOXJ1^{low} ciliated cells were the only population to have significant activity in "TNF signaling" (Fig. 7F). There were 15 shared age-associated differences in pathways all clusters, and an additional 31 shared pathways between all clusters excluding the smaller ionocyte population (Fig. 7E). Club and basal cells had the most differences between age cohorts, and shared the most differentially active pathways (Fig. 7E). There were dramatic differences in the "ISGs" and "Antigen processing and presentation" pathways in all major cell populations (both ciliated cell clusters, club cells, and basal cells), "Coronavirus disease" in club cells and FOXJ1^{low} ciliated cells, and "Type 1 IFNs" in club cells only (SFig. 10).

bioRxiv preprint doi: https://doi.org/10.1101/2024.04.02.587663; this version posted April 2, 2024. The copyright holder for this preprint (which was not certified by peer review) is the author/funder, who has granted bioRxiv a license to display the preprint in perpetuity. It is made available under aCC-BY 4.0 International license.

Discussion

Understanding the host response to SARS-CoV-2 infection is critical in developing effective strategies for preventing and treating COVID-19. The lung epithelium is the primary target of SARS-CoV-2 infection, and early prevention strategies targeting these cells can therefore be expected to determine disease severity and outcome. Inefficient or dysregulated host responses to SARS-CoV-2 infection in lung epithelial cells can lead to severe lung damage and respiratory failure, which are the leading causes of mortality in COVID-19 patients. Moreover, some of the earliest epidemiological evidence from the COVID-19 pandemic showed that age is a significant risk factor for severe COVID-19 (47-50). Therefore, investigating age-related host responses in lung epithelial cells is crucial for understanding the underlying mechanisms of increased susceptibility, pathogenesis, and severity of COVID-19 in different populations. Here, we employed single-cell RNA sequencing (scRNA-seq) to investigate the transcriptomic profiles of primary lung epithelial cells from pediatric and adult populations in response to SARS-CoV-2. Our scRNA-seq analysis revealed six cell types in air-liquid interface cultures derived from primary human lung tissue: two ciliated cell types ($FOXJ1^{low}$ and $FOXJ1^{high}$), club cells, basal cells, multiciliated precursors, and ionocytes (Fig. 1).

Trajectory and pseudotime analysis were used to investigate the differentiation pathways of various cell types in our cell culture system. Basal cells are known as the most “stem-like” cells in the lung epithelium (43, 44). Trajectory analysis showed that basal cells differentiated into all of the other cell populations and confirmed that the ciliated cell populations were not two

bioRxiv preprint doi: https://doi.org/10.1101/2024.04.02.587663; this version posted April 2, 2024. The copyright holder for this preprint (which was not certified by peer review) is the author/funder, who has granted bioRxiv a license to display the preprint in perpetuity. It is made available under aCC-BY 4.0 International license.

479 distinct branches of ciliated cells; instead, they were at different levels of differentiation, with
480 FOXJ1^{high} ciliated cells being the most terminally differentiated. Density plots of 7 canonical
481 ciliated cell markers confirmed that the most differentiated ciliated cells were located within the
482 FOXJ1^{high} ciliated cell cluster (SFig. 10).

483 One drawback of using scRNA-seq analysis to understand viral infections on adherent
484 cells is the absence of spatial data. This is especially true as infection-induced paracrine
485 signaling elicits responses in the neighboring cells. Cell-cell communication analysis attempts to
486 recapitulate multicellular coordination by inferring intercellular communication from the
487 expression of genes associated with such communication (25). Using aggregated scores from
488 various cell-cell communication methods, we found that FOXJ1^{low} ciliated cells had very little
489 interpopulation and intrapopulation communication. While we expected cell communication
490 patterns or expression of specific ligand-receptor pairs to change between infected and
491 uninfected samples, no significant differences were observed. Notably, age was a significant
492 factor in communication patterns (Fig. 3E)(Fig. 3F). Overall, footprint analysis of the ligand-
493 receptor pairs in the factors that were different between age cohorts revealed that adult donors
494 were more associated with cell communication patterns that resulted in signaling leading to high
495 NFκB activity, and low MAPK, PI3K, and TRAIL activity in the adult donors (Fig. 3G). To our
496 knowledge, this finding is novel in human age-related pulmonary biology.

497 Our data reveals cluster-specific differences in adult and pediatric samples (SFig. 8).
498 When splitting the groups by infection status to remove infection-related variability, we were
499 surprised to find that age-related differences were more prevalent in uninfected samples
500 compared to infected samples in every cluster (Fig. 4A)(Fig. 4B)(Fig.S10). We found that the
501 geneset for “Coronavirus disease” was differentially enriched between the age cohorts in both

bioRxiv preprint doi: https://doi.org/10.1101/2024.04.02.587663; this version posted April 2, 2024. The copyright holder for this preprint (which was not certified by peer review) is the author/funder, who has granted bioRxiv a license to display the preprint in perpetuity. It is made available under aCC-BY 4.0 International license.

mock and infected samples in FOXJ1^{low} ciliated cells and club cells, while FOXJ1^{high} ciliated and basal cells only had age-related enrichment in the infected samples (Fig. 4B)(Fig. 4D)(Fig. 4F)(Fig. 4H). Generally, we interpreted this age-related

Similar to recent publications assessing the expression of SARS-CoV-2 entry factors along the airway epithelium, we found that our cells had very low expression of ACE2, TMPRSS2, NRP1, AXL, FURIN, and CTSL entry factor genes (Fig. 5A)(14, 51). Although this low expression was sufficient for SARS-CoV-2 infection in all cell populations, with the majority of infected cells belonging to the FOXJ1^{low} ciliated cell population (Fig. 5B)(Fig. 5D). However, FOXJ1^{high} ciliated cells showed the most robust responses to infection and followed more canonical antiviral signaling responses (Fig. 5D)(Fig. 7A) (Fig. 7F). Overall, FOXJ1^{low} ciliated cells seem to have inhibited transcription at the global level, leading to little overlap between the DEGs after infection between the two ciliated cell populations (Fig. 6A)(Fig. 5E).

The stark differences in the ciliated cell population's response to SARS-CoV-2 prompted us to compare the ciliated cell types to understand the pathogenic phenotype of the FOXJ1^{low} ciliated cells. We found that FOXJ1^{low} ciliated cells were more metabolically active, while FOXJ1^{high} ciliated cells were more active in cilium motility and ciliogenesis. Other studies have shown that SARS-CoV-2 may induce a marginal upregulation in metabolic activity (52, 53). Interestingly, the differences in axoneme assembly, ciliogenesis, dynein binding, and microtubule motor activity mirrored the microanatomy of 9+2 vs. 9+0 cilium modalities (Fig. 6A)(Fig. 6B). FOXJ1^{high} ciliated cells were more similar to the microanatomy of motile cilia. In contrast, FOXJ1^{low} ciliated cells aligned more with primary or nodal cilium (Fig. 6B). Using scanning electron microscopy, other groups have found that low FOXJ1 expression in ciliated cells is associated with a reduction in motile cilia and mucociliary clearance functionality

bioRxiv preprint doi: https://doi.org/10.1101/2024.04.02.587663; this version posted April 2, 2024. The copyright holder for this preprint (which was not certified by peer review) is the author/funder, who has granted bioRxiv a license to display the preprint in perpetuity. It is made available under aCC-BY 4.0 International license.

525 through impairments of cilia sweeping coordination (54, 55). However, our trajectory and cell
526 phase analysis show similar proportions of FOXJ1^{low} cells in mock and infected samples.
527 Previous studies have shown that lung injury, through various means, can cause the
528 dedifferentiation of ciliated cells and reduced FOXJ1 expression (41, 42, 44, 55-57). The process
529 for obtaining primary lung epithelial cells on an air-liquid interface is strenuous in itself and
530 could be a latent factor in these models. This may be important in that FOXJ1^{low} ciliated cells
531 could be transient and only present after lung injury (or cellular stress, in our *in vitro* model);
532 whether or not these ciliated cell types are abundant in healthy lung tissue remains to be seen
533 (15, 17, 18, 58, 59). However, there has been some evidence that ciliated cells with low
534 expression of FOXJ1 are associated with Bronchiectasis, a condition where the walls of the
535 bronchi are thickened from inflammation and infection (60).

536 We found that traditional gene enrichment methods using a one-sided Fisher's Exact Test
537 or a Hypergeometric test using differentially expressed genes yielded few enriched pathways.
538 However, updated rank-based methods significantly reduced false negatives due to intercellular
539 and inter-sample variability. In addition, these methods captured significant functional
540 differences in our comparative analyses on the effects of age and infection status (Fig. 7D)(Fig.
541 7E). This was particularly important when investigating common antiviral signaling pathways.

542 Interferon signaling through interferon expression and the induction of hundreds of
543 interferon-stimulated genes (ISGs) is well-documented to be an antiviral protective mechanism;
544 ISGs suppress viral replication and activation of downstream immune signaling (6, 11, 39, 40,
545 61-68). However, many studies have found very few known interferon-related genes to be
546 expressed after SARS-CoV-2 infection (2-6, 11, 68-70). In our study, we utilized a geneset of
547 previously published ISGs with rank-based scoring to examine indirect type I and type III

bioRxiv preprint doi: https://doi.org/10.1101/2024.04.02.587663; this version posted April 2, 2024. The copyright holder for this preprint (which was not certified by peer review) is the author/funder, who has granted bioRxiv a license to display the preprint in perpetuity. It is made available under aCC-BY 4.0 International license.

548 interferon signaling (39, 40). Using this method, we found significant interferon signaling in a
549 broader sense when examining the breadth of genes associated with an interferon response,
550 rather than induction of type I and III interferon genes in isolation (Fig. 7F). After infection, the
551 host response patterns for ciliated cell types were vastly different. FOXJ1^{high} ciliated cells
552 exhibited expression patterns more similar to club cells while FOXJ1^{low} ciliated cells were more
553 similar to basal cells. This suggests that more transient cell types of the lung epithelium may
554 have a muted response to SARS-CoV-2.

555 Some limitations of this study include limited donors. Thus, while many of the age-
556 related differences are significant for our cohort, larger future sample sizes may give us more
557 insight into these differences. Additionally, this study relies entirely on RNA and does not
558 include any protein data. Without protein data, the actual functional outcomes of SARS-CoV-2
559 infection cannot be inferred because the presence of RNA does not necessarily correlate with
560 protein expression; SARS-CoV-2 and other viral pathogens typically have mechanisms that
561 interfere with protein translation (71, 72). Nevertheless, our findings provide important insights
562 into the cellular and molecular mechanisms of SARS-CoV-2 infection in lower lung epithelial
563 cells. Specifically, we found that cellular responses to the virus vastly differ between cell types,
564 highlighting the importance of targeted approaches in developing effective therapeutics and
565 prevention strategies for COVID-19.

566 # Data availability statement

567 The datasets presented in this study were deposited in the National Center for
568 Biotechnology Information's Gene Expression Omnibus database and are available upon request.

bioRxiv preprint doi: https://doi.org/10.1101/2024.04.02.587663; this version posted April 2, 2024. The copyright holder for this preprint (which was not certified by peer review) is the author/funder, who has granted bioRxiv a license to display the preprint in perpetuity. It is made available under aCC-BY 4.0 International license.

569

570 Acknowledgments

571 The authors want to acknowledge the contributions of Gloria Pryhuber and the LungMAP
572 Biorepository (BRINDL), John Ashton and Michelle Zanche from the UR Genomics Research
573 Center (GRC), Martin Pavelka Jr. and Sonia Rosenberger from the UR Biosafety Level 3 (BSL3)
574 facility and the UR's Institutional Biosafety Committee (IBC). In addition, the authors would
575 like to acknowledge the advice and support of Mukta G. Palshikar.

576

bioRxiv preprint doi: https://doi.org/10.1101/2024.04.02.587663; this version posted April 2, 2024. The copyright holder for this preprint (which was not certified by peer review) is the author/funder, who has granted bioRxiv a license to display the preprint in perpetuity. It is made available under aCC-BY 4.0 International license.

References

1. Harrison AG, Lin T, Wang P. Mechanisms of SARS-CoV-2 transmission and pathogenesis. Trends in immunology. 2020;41(12):1100-15.

2. Sa Ribero M, Jouvenet N, Dreux M, Nisole S. Interplay between SARS-CoV-2 and the type I interferon response. PLoS pathogens. 2020;16(7):e1008737.

3. Kim Y-M, Shin E-C. Type I and III interferon responses in SARS-CoV-2 infection. Experimental & molecular medicine. 2021;53(5):750-60.

4. King C, Sprent J. Dual nature of type I interferons in SARS-CoV-2-induced inflammation. Trends in immunology. 2021;42(4):312-22.

5. Blanco-Melo D, Nilsson-Payant BE, Liu W-C, Uhl S, Hoagland D, Møller R, et al. Imbalanced host response to SARS-CoV-2 drives development of COVID-19. Cell. 2020;181(5):1036-45. e9.

6. Cooper MA, Fehniger TA, Ponnappan A, Mehta V, Wewers MD, Caligiuri MA. Interleukin-1β costimulates interferon-γ production by human natural killer cells. European journal of immunology. 2001;31(3):792-801.

7. Smits SL, De Lang A, Van Den Brand JM, Leijten LM, Van Ijcken WF, Eijkemans MJ, et al. Exacerbated innate host response to SARS-CoV in aged non-human primates. PLoS pathogens. 2010;6(2):e1000756.

8. Yonker LM, Neilan AM, Bartsch Y, Patel AB, Regan J, Arya P, et al. Pediatric severe acute respiratory syndrome coronavirus 2 (SARS-CoV-2): clinical presentation, infectivity, and immune responses. The Journal of pediatrics. 2020;227:45-52. e5.

9. Payne AB, Gilani Z, Godfred-Cato S, Belay ED, Feldstein LR, Patel MM, et al. Incidence of multisystem inflammatory syndrome in children among US persons infected with SARS-CoV-2. JAMA network open. 2021;4(6):e2116420-e.

10. Holm M, Hartling UB, Schmidt LS, Glenthøj JP, Kruse A, Rytter MH, et al. Multisystem inflammatory syndrome in children occurred in one of four thousand children with severe acute respiratory syndrome coronavirus 2. Acta Paediatrica (Oslo, Norway: 1992). 2021;110(9):2581.

11. Hatton CF, Botting RA, Dueñas ME, Haq IJ, Verdon B, Thompson BJ, et al. Delayed induction of type I and III interferons mediates nasal epithelial cell permissiveness to SARS-CoV-2. Nature Communications. 2021;12(1):7092.

bioRxiv preprint doi: https://doi.org/10.1101/2024.04.02.587663; this version posted April 2, 2024. The copyright holder for this preprint (which was not certified by peer review) is the author/funder, who has granted bioRxiv a license to display the preprint in perpetuity. It is made available under aCC-BY 4.0 International license.

12. Hu Y, Li W, Gao T, Cui Y, Jin Y, Li P, et al. The severe acute respiratory syndrome coronavirus nucleocapsid inhibits type I interferon production by interfering with TRIM25-mediated RIG-I ubiquitination. Journal of virology. 2017;91(8):e02143-16.

13. Ravindra NG, Alfajaro MM, Gasque V, Huston NC, Wan H, Szigeti-Buck K, et al. Single-cell longitudinal analysis of SARS-CoV-2 infection in human airway epithelium identifies target cells, alterations in gene expression, and cell state changes. PLoS biology. 2021;19(3):e3001143.

14. Muus C, Luecken MD, Eraslan G, Sikkema L, Waghray A, Heimberg G, et al. Single-cell meta-analysis of SARS-CoV-2 entry genes across tissues and demographics. Nature medicine. 2021;27(3):546-59.

15. Wang Q, Bhattacharya S, Mereness JA, Anderson C, Lillis JA, Misra RS, et al. A novel in vitro model of primary human pediatric lung epithelial cells. Pediatric research. 2020;87(3):511-7.

16. Anderson CS, Chirkova T, Slaunwhite CG, Qiu X, Walsh EE, Anderson LJ, et al. CX3CR1 Engagement by Respiratory Syncytial Virus Leads to Induction of Nucleolin and Dysregulation of Cilium-Related Genes. Journal of Virology. 2021;95(11):e00095-21.

17. Osborn RM, Leach J, Zanche M, Ashton JM, Chu C, Thakar J, et al. SARS-CoV-2 inactivation and scRNAseq sample preparation protocol. 2023.

18. Osborn RM, Leach J, Zanche M, Ashton JM, Chu C, Thakar J, et al. Preparation of noninfectious scRNAseq samples from SARS-CoV-2-infected epithelial cells. Plos one. 2023;18(2):e0281898.

19. Hao Y, Hao S, Andersen-Nissen E, Mauck III WM, Zheng S, Butler A, et al. Integrated analysis of multimodal single-cell data. Cell. 2021;184(13):3573-87. e29.

20. Chen J, Bardes EE, Aronow BJ, Jegga AG. ToppGene Suite for gene list enrichment analysis and candidate gene prioritization. Nucleic acids research. 2009;37(suppl_2):W305-W11.

21. Wu T, Hu E, Xu S, Chen M, Guo P, Dai Z, et al. clusterProfiler 4.0: A universal enrichment tool for interpreting omics data. The Innovation. 2021;2(3):100141.

22. Ianevski A, Giri AK, Aittokallio T. Fully-automated and ultra-fast cell-type identification using specific marker combinations from single-cell transcriptomic data. Nature communications. 2022;13(1):1246.

23. Bunis DG, Andrews J, Fragiadakis GK, Burt TD, Sirota M. dittoSeq: universal user-friendly single-cell and bulk RNA sequencing visualization toolkit. Bioinformatics. 2020;36(22-23):5535-6.

bioRxiv preprint doi: https://doi.org/10.1101/2024.04.02.587663; this version posted April 2, 2024. The copyright holder for this preprint (which was not certified by peer review) is the author/funder, who has granted bioRxiv a license to display the preprint in perpetuity. It is made available under aCC-BY 4.0 International license.

24. Trapnell C, Cacchiarelli D, Grimsby J, Pokharel P, Li S, Morse M, et al. The dynamics and regulators of cell fate decisions are revealed by pseudotemporal ordering of single cells. Nature biotechnology. 2014;32(4):381-6.

25. Dimitrov D, Türei D, Garrido-Rodriguez M, Burmedi PL, Nagai JS, Boys C, et al. Comparison of methods and resources for cell-cell communication inference from single-cell RNA-Seq data. Nature Communications. 2022;13(1):3224.

26. Kolde R, Laur S, Adler P, Vilo J. Robust rank aggregation for gene list integration and meta-analysis. Bioinformatics. 2012;28(4):573-80.

27. Raredon MSB, Yang J, Garritano J, Wang M, Kushnir D, Schupp JC, et al. Computation and visualization of cell–cell signaling topologies in single-cell systems data using connectome. Scientific Reports. 2022;12(1):4187.

28. Cabello-Aguilar S, Alame M, Kon-Sun-Tack F, Fau C, Lacroix M, Colinge J. SingleCellSignalR: inference of intercellular networks from single-cell transcriptomics. Nucleic Acids Research. 2020;48(10):e55-e.

29. Wang Y, Wang R, Zhang S, Song S, Jiang C, Han G, et al. iTALK: an R package to characterize and illustrate intercellular communication. BioRxiv. 2019:507871.

30. Efremova M, Vento-Tormo M, Teichmann SA, Vento-Tormo R. CellPhoneDB: inferring cell–cell communication from combined expression of multi-subunit ligand–receptor complexes. Nature protocols. 2020;15(4):1484-506.

31. Hou R, Denisenko E, Ong HT, Ramilowski JA, Forrest AR. Predicting cell-to-cell communication networks using NATMI. Nature communications. 2020;11(1):5011.

32. Armingol E, Baghdassarian HM, Martino C, Perez-Lopez A, Aamodt C, Knight R, et al. Context-aware deconvolution of cell–cell communication with Tensor-cell2cell. Nature communications. 2022;13(1):3665.

33. Badia-i-Mompel P, Vélez Santiago J, Braunger J, Geiss C, Dimitrov D, Müller-Dott S, et al. decoupleR: ensemble of computational methods to infer biological activities from omics data. Bioinformatics Advances. 2022;2(1):vbac016.

34. Schubert M, Klinger B, Klünemann M, Sieber A, Uhlitz F, Sauer S, et al. Perturbation-response genes reveal signaling footprints in cancer gene expression. Nature communications. 2018;9(1):20.

35. Finak G, McDavid A, Yajima M, Deng J, Gersuk V, Shalek AK, et al. MAST: a flexible statistical framework for assessing transcriptional changes and characterizing heterogeneity in single-cell RNA sequencing data. Genome biology. 2015;16(1):1-13.

36. Conway JR, Lex A, Gehlenborg N. UpSetR: an R package for the visualization of intersecting sets and their properties. Bioinformatics. 2017.

bioRxiv preprint doi: https://doi.org/10.1101/2024.04.02.587663; this version posted April 2, 2024. The copyright holder for this preprint (which was not certified by peer review) is the author/funder, who has granted bioRxiv a license to display the preprint in perpetuity. It is made available under aCC-BY 4.0 International license.

679 37. Krassowski M, Arts M, Lagger C. Krassowski/Complex-Upset: v1. 3.3. Zenodo
680 2020Available online. 2020;10.

681 38. Kanehisa M, Goto S. KEGG: kyoto encyclopedia of genes and genomes. Nucleic acids
682 research. 2000;28(1):27-30.

683 39. Schoggins JW, Rice CM. Interferon-stimulated genes and their antiviral effector
684 functions. Current opinion in virology. 2011;1(6):519-25.

685 40. Schoggins JW, Wilson SJ, Panis M, Murphy MY, Jones CT, Bieniasz P, et al. A diverse
686 range of gene products are effectors of the type I interferon antiviral response. Nature.
687 2011;472(7344):481-5.

688 41. Chen F, Fine A. Stem cells in lung injury and repair. The American journal of pathology.
689 2016;186(10):2544-50.

690 42. Tata PR, Mou H, Pardo-Saganta A, Zhao R, Prabhu M, Law BM, et al. Dedifferentiation
691 of committed epithelial cells into stem cells in vivo. Nature. 2013;503(7475):218-23.

692 43. Wu M, Zhang X, Lin Y, Zeng Y. Roles of airway basal stem cells in lung homeostasis
693 and regenerative medicine. Respiratory Research. 2022;23(1):1-12.

694 44. Rock JR, Onaitis MW, Rawlins EL, Lu Y, Clark CP, Xue Y, et al. Basal cells as stem
695 cells of the mouse trachea and human airway epithelium. Proceedings of the National
696 Academy of Sciences. 2009;106(31):12771-5.

697 45. Mazumdar J, Hickey MM, Pant DK, Durham AC, Sweet-Cordero A, Vachani A, et al.
698 HIF-2α deletion promotes Kras-driven lung tumor development. Proceedings of the
699 National Academy of Sciences. 2010;107(32):14182-7.

700 46. Reynolds SD, Reynolds PR, Pryhuber GS, Finder JD, Stripp BR. Secretoglobins
701 SCGB3A1 and SCGB3A2 define secretory cell subsets in mouse and human airways.
702 American journal of respiratory and critical care medicine. 2002;166(11):1498-509.

703 47. Fialkowski A, Gernez Y, Arya P, Weinacht KG, Kinane TB, Yonker LM. Insight into the
704 pediatric and adult dichotomy of COVID-19: age-related differences in the immune
705 response to SARS-CoV-2 infection. Pediatric Pulmonology. 2020;55(10):2556-64.

706 48. Wu JT, Leung K, Bushman M, Kishore N, Niehus R, de Salazar PM, et al. Estimating
707 clinical severity of COVID-19 from the transmission dynamics in Wuhan, China. Nature
708 medicine. 2020;26(4):506-10.

709 49. Gallo Marin B, Aghagoli G, Lavine K, Yang L, Siff EJ, Chiang SS, et al. Predictors of
710 COVID-19 severity: a literature review. Reviews in medical virology. 2021;31(1):1-10.

711 50. Pijls BG, Jolani S, Atherley A, Derckx RT, Dijkstra JI, Franssen GH, et al. Demographic
712 risk factors for COVID-19 infection, severity, ICU admission and death: a meta-analysis
713 of 59 studies. BMJ open. 2021;11(1):e044640.

bioRxiv preprint doi: https://doi.org/10.1101/2024.04.02.587663; this version posted April 2, 2024. The copyright holder for this preprint (which was not certified by peer review) is the author/funder, who has granted bioRxiv a license to display the preprint in perpetuity. It is made available under aCC-BY 4.0 International license.

51. Sungnak W, Huang N, Bécavin C, Berg M, Queen R, Litvinukova M, et al. SARS-CoV-2 entry factors are highly expressed in nasal epithelial cells together with innate immune genes. Nature medicine. 2020;26(5):681-7.

52. Ehrlich A, Uhl S, Ioannidis K, Hofree M, tenOever BR, Nahmias Y. The SARS-CoV-2 transcriptional metabolic signature in lung epithelium. Available at SSRN 3650499. 2020.

53. Gassen NC, Papies J, Bajaj T, Emanuel J, Dethloff F, Chua RL, et al. SARS-CoV-2-mediated dysregulation of metabolism and autophagy uncovers host-targeting antivirals. Nature communications. 2021;12(1):3818.

54. Robinot R, Hubert M, de Melo GD, Lazarini F, Bruel T, Smith N, et al. SARS-CoV-2 infection damages airway motile cilia and impairs mucociliary clearance. BioRxiv. 2020.

55. Robinot R, Hubert M, de Melo GD, Lazarini F, Bruel T, Smith N, et al. SARS-CoV-2 infection induces the dedifferentiation of multiciliated cells and impairs mucociliary clearance. Nature communications. 2021;12(1):4354.

56. Davis JD, Wypych TP. Cellular and functional heterogeneity of the airway epithelium. Mucosal immunology. 2021;14(5):978-90.

57. Rawlins EL, Ostrowski LE, Randell SH, Hogan BL. Lung development and repair: contribution of the ciliated lineage. Proceedings of the National Academy of Sciences. 2007;104(2):410-7.

58. de Jong PM, van Sterkenburg MA, Hesseling SC, Kempenaar JA, Mulder AA, Mommaas AM, et al. Ciliogenesis in human bronchial epithelial cells cultured at the air-liquid interface. American journal of respiratory cell and molecular biology. 1994;10(3):271-7.

59. Bandyopadhyay G, Huyck HL, Misra RS, Bhattacharya S, Wang Q, Mereness J, et al. Dissociation, cellular isolation, and initial molecular characterization of neonatal and pediatric human lung tissues. American Journal of Physiology-Lung Cellular and Molecular Physiology. 2018;315(4):L576-L83.

60. Zou XL, Yang HL, Ding WW, Li HK, Zhou YQ, Zhang TT. Down-expression of Foxj1 on airway epithelium with impaired cilia architecture in non-cystic fibrosis bronchiectasis implies disease severity. The Clinical Respiratory Journal. 2023;17(5):405-13.

61. Ioannidis I, Ye F, McNally B, Willette M, Flaño E. Toll-like receptor expression and induction of type I and type III interferons in primary airway epithelial cells. Journal of virology. 2013;87(6):3261-70.

62. Kerkar SP, Chinnasamy D, Hadi N, Melenhorst J, Muranski P, Spyridonidis A, et al. Timing and intensity of exposure to interferon-γ critically determines the function of monocyte-derived dendritic cells. Immunology. 2014;143(1):96-108.

bioRxiv preprint doi: https://doi.org/10.1101/2024.04.02.587663; this version posted April 2, 2024. The copyright holder for this preprint (which was not certified by peer review) is the author/funder, who has granted bioRxiv a license to display the preprint in perpetuity. It is made available under aCC-BY 4.0 International license.

63. Gessani S, Conti L, Del Cornò M, Belardelli F. Type I interferons as regulators of human antigen presenting cell functions. Toxins. 2014;6(6):1696-723.

64. Wu W, Zhang W, Duggan ES, Booth JL, Zou M-H, Metcalf JP. RIG-I and TLR3 are both required for maximum interferon induction by influenza virus in human lung alveolar epithelial cells. Virology. 2015;482:181-8.

65. Wack A, Terczyńska-Dyla E, Hartmann R. Guarding the frontiers: the biology of type III interferons. Nature immunology. 2015;16(8):802-9.

66. Schoggins JW. Recent advances in antiviral interferon-stimulated gene biology. F1000Research. 2018;7.

67. Kak G, Raza M, Tiwari BK. Interferon-gamma (IFN-γ): exploring its implications in infectious diseases. Biomolecular concepts. 2018;9(1):64-79.

68. Sacchi A, Giannessi F, Sabatini A, Percario ZA, Affabris E. SARS-CoV-2 Evasion of the Interferon System: Can We Restore Its Effectiveness? International Journal of Molecular Sciences. 2023;24(11):9353.

69. Zheng Y, Zhuang M-W, Han L, Zhang J, Nan M-L, Zhan P, et al. Severe acute respiratory syndrome coronavirus 2 (SARS-CoV-2) membrane (M) protein inhibits type I and III interferon production by targeting RIG-I/MDA-5 signaling. Signal transduction and targeted therapy. 2020;5(1):1-13.

70. Min Y-Q, Huang M, Sun X, Deng F, Wang H, Ning Y-J. Immune evasion of SARS-CoV-2 from interferon antiviral system. Computational and structural biotechnology journal. 2021;19:4217-25.

71. Pan JA, Peng X, Gao Y, Li Z, Lu X, Chen Y, et al. Genome-wide analysis of protein-protein interactions and involvement of viral proteins in SARS-CoV replication. PloS one. 2008;3(10):e3299.

72. Finkel Y, Gluck A, Nachshon A, Winkler R, Fisher T, Rozman B, et al. SARS-CoV-2 uses a multipronged strategy to impede host protein synthesis. Nature. 2021;594(7862):240-5.

bioRxiv preprint doi: https://doi.org/10.1101/2024.04.02.587663; this version posted April 2, 2024. The copyright holder for this preprint (which was not certified by peer review) is the author/funder, who has granted bioRxiv a license to display the preprint in perpetuity. It is made available under aCC-BY 4.0 International license.

Main Figures

bioRxiv preprint doi: https://doi.org/10.1101/2024.04.02.587663; this version posted April 2, 2024. The copyright holder for this preprint (which was not certified by peer review) is the author/funder, who has granted bioRxiv a license to display the preprint in perpetuity. It is made available under aCC-BY 4.0 International license.

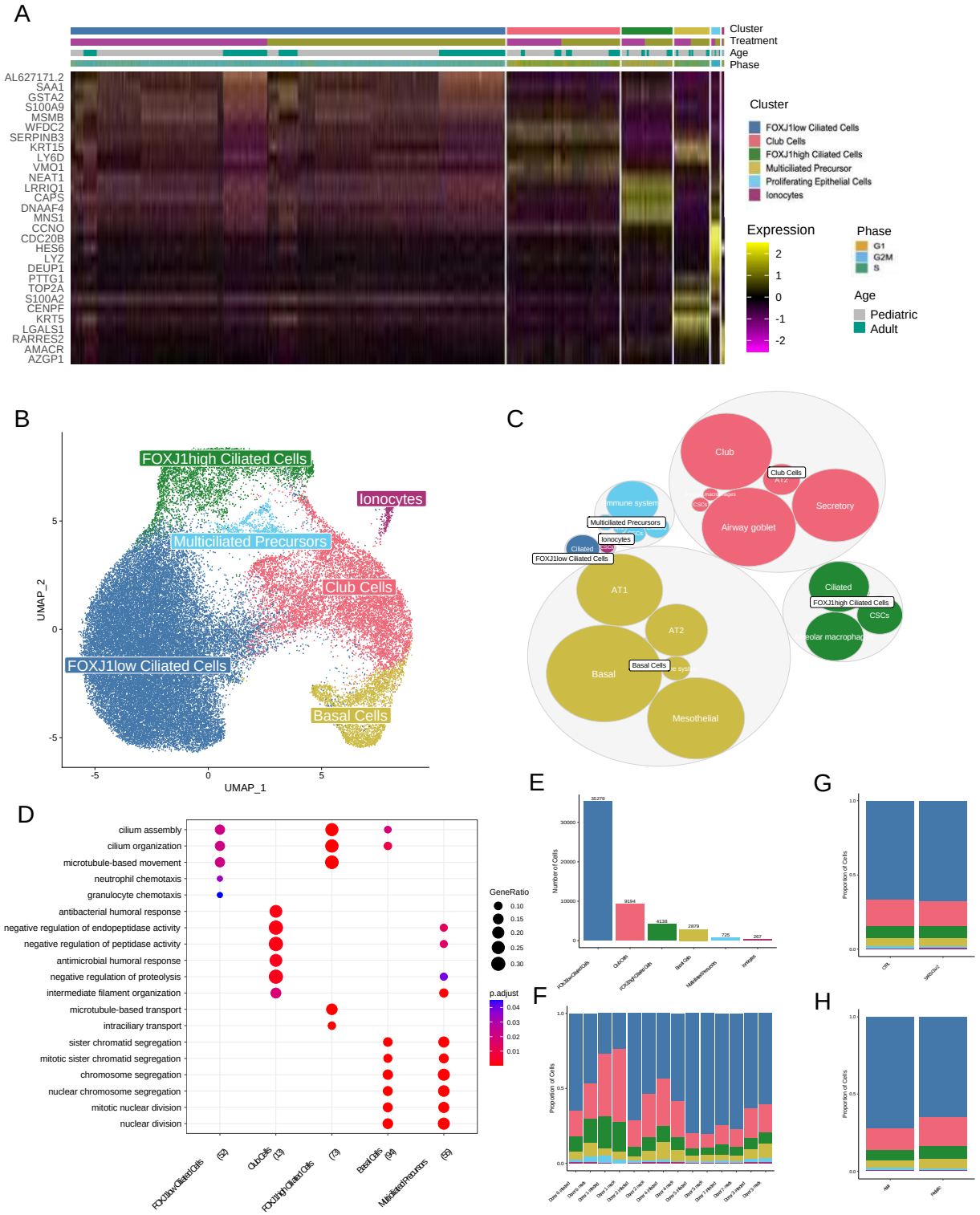

783

784 **Fig 1. Clustering and annotation of scRNA-seq data from primary lung epithelial cells.** (A)

785 Heatmap of integrated gene expression of cluster markers from 52,482 cells annotated by

bioRxiv preprint doi: https://doi.org/10.1101/2024.04.02.587663; this version posted April 2, 2024. The copyright holder for this preprint (which was not certified by peer review) is the author/funder, who has granted bioRxiv a license to display the preprint in perpetuity. It is made available under aCC-BY 4.0 International license.

786 assigned cluster, treatment status, donor age category, and cell cycle phase. (B) Uniform
787 Manifold Approximation and Projection (UMAP) of all cells colored by cluster annotation. (C)
788 Circular treemap of cell annotations. Circles are colored and clustered by higher-level
789 annotations, and subclustered sizes are a function of the number of cells assigned to the
790 subcluster. (D) Gene ontology (GO) analysis of cluster markers using Biological Process terms.
791 (E) Bar plot of cell number in each cluster. (F) Stacked bar plot of cluster proportions for each
792 sample. (G) Stacked bar plot of cluster proportions by treatment status. (H) Stacked bar plot of
793 cluster proportions by age category.

794

795
796

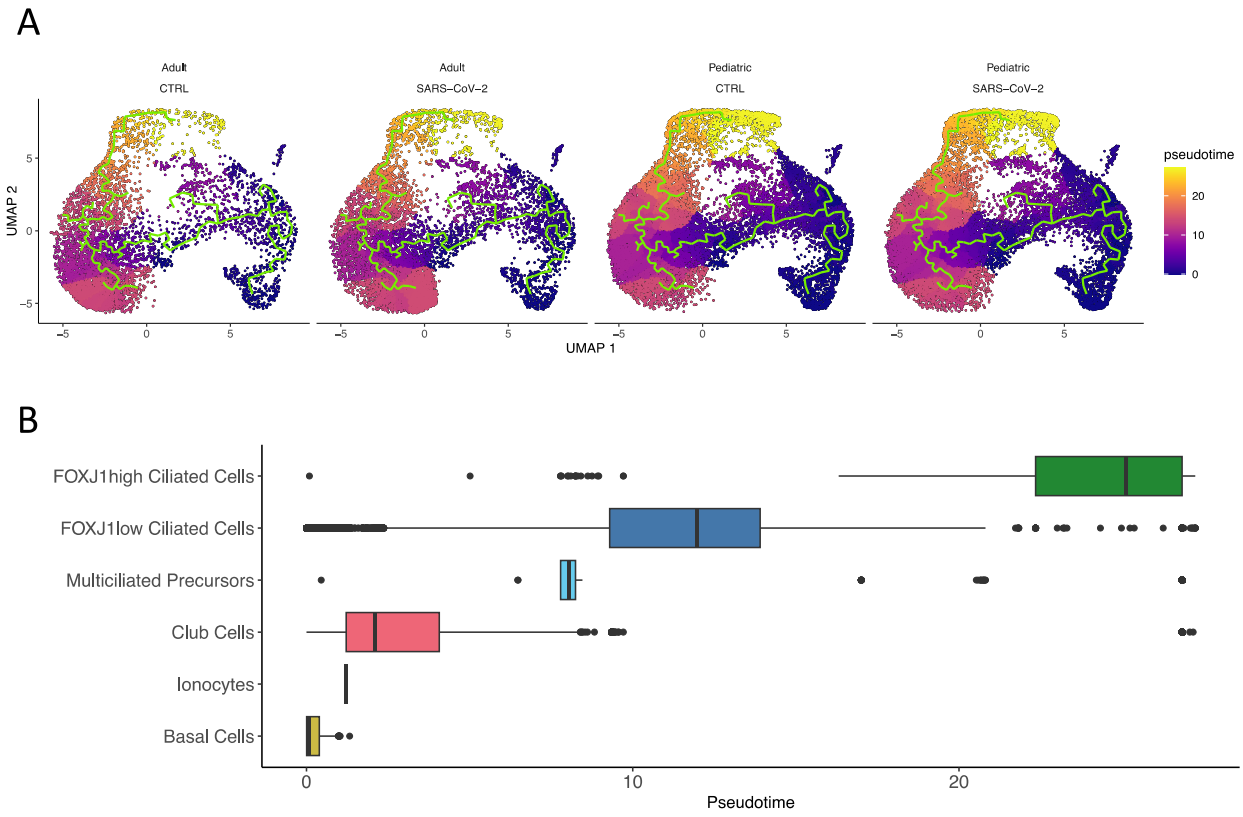

797

bioRxiv preprint doi: https://doi.org/10.1101/2024.04.02.587663; this version posted April 2, 2024. The copyright holder for this preprint (which was not certified by peer review) is the author/funder, who has granted bioRxiv a license to display the preprint in perpetuity. It is made available under aCC-BY 4.0 International license.

798 **Fig 2. Trajectory analysis and pseudotime comparisons.** (A) UMAPs separated by covariates
799 with calculated trajectory in chartreuse, and colored by pseudotime representing differentiation
800 from dark blue to yellow (more differentiated). (B) Boxplots of the range of pseudotime in each
801 cluster, colored by cluster annotation shown in Figure 1.

802

bioRxiv preprint doi: https://doi.org/10.1101/2024.04.02.587663; this version posted April 2, 2024. The copyright holder for this preprint (which was not certified by peer review) is the author/funder, who has granted bioRxiv a license to display the preprint in perpetuity. It is made available under aCC-BY 4.0 International license.

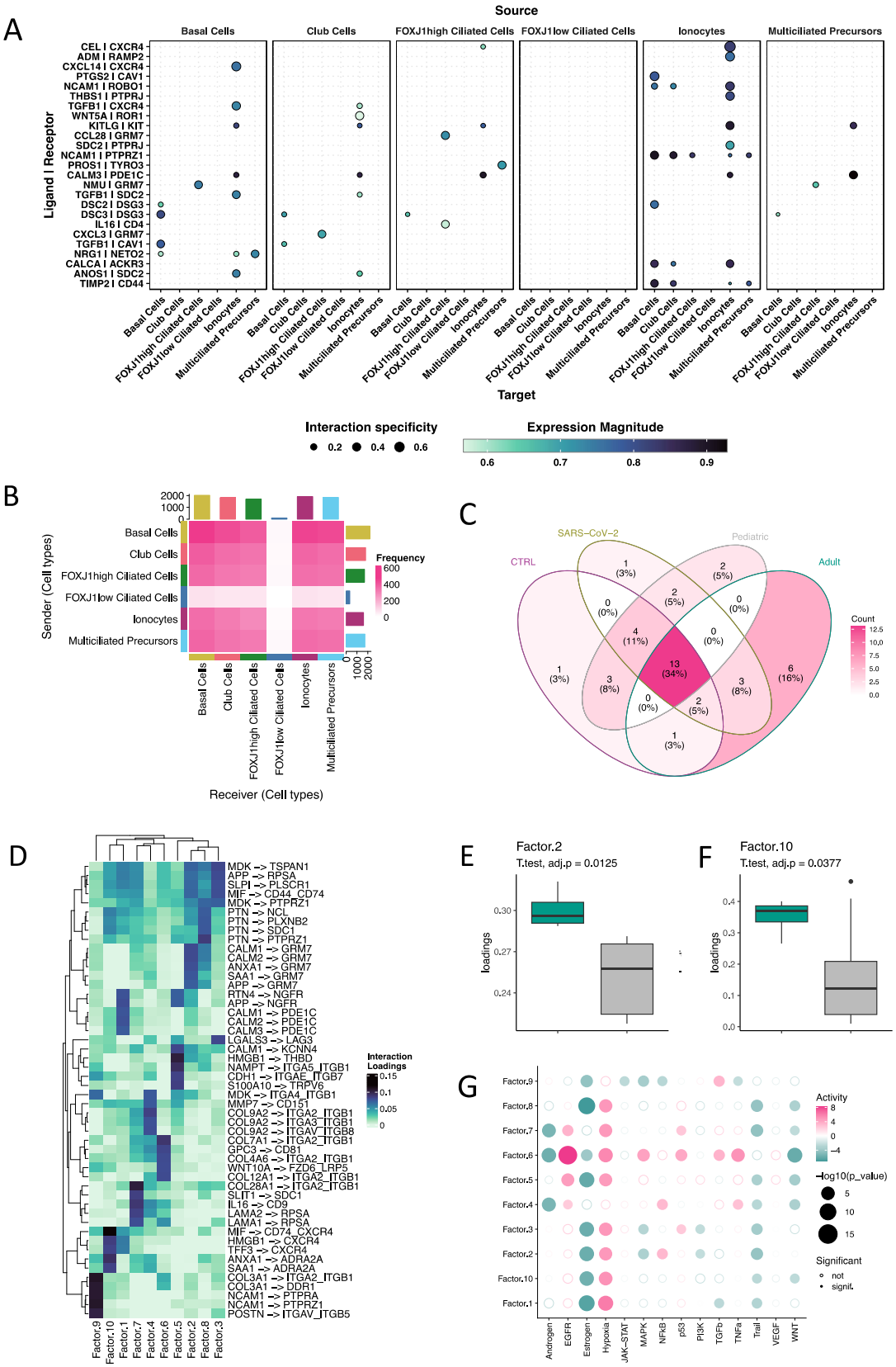

bioRxiv preprint doi: https://doi.org/10.1101/2024.04.02.587663; this version posted April 2, 2024. The copyright holder for this preprint (which was not certified by peer review) is the author/funder, who has granted bioRxiv a license to display the preprint in perpetuity. It is made available under aCC-BY 4.0 International license.

804 **Fig 3. Cell-cell communication analysis. (**A) Dot plots of ligand-receptor pairs (y-axis) show
805 the source cell type sending the signal on top and the receiving cell populations on the bottom.
806 (B) Heatmap of the frequencies of interactions for each pair of potentially communicating cell
807 types. Annotation bar plot on top ("receiving") and right ("sending") is the total number of
808 interactions per cell type. (C) Venn diagram of top 25 ligand-receptor pairs across infection and
809 age. (D) Heatmap of top 5 ligand-receptor loadings for each Factor. (E and F) Boxplots of age-
810 related factor loadings with adult samples in green and pediatric samples in grey. (G) Dotplot of
811 footprint enrichment analysis of downstream pathways.

812
813

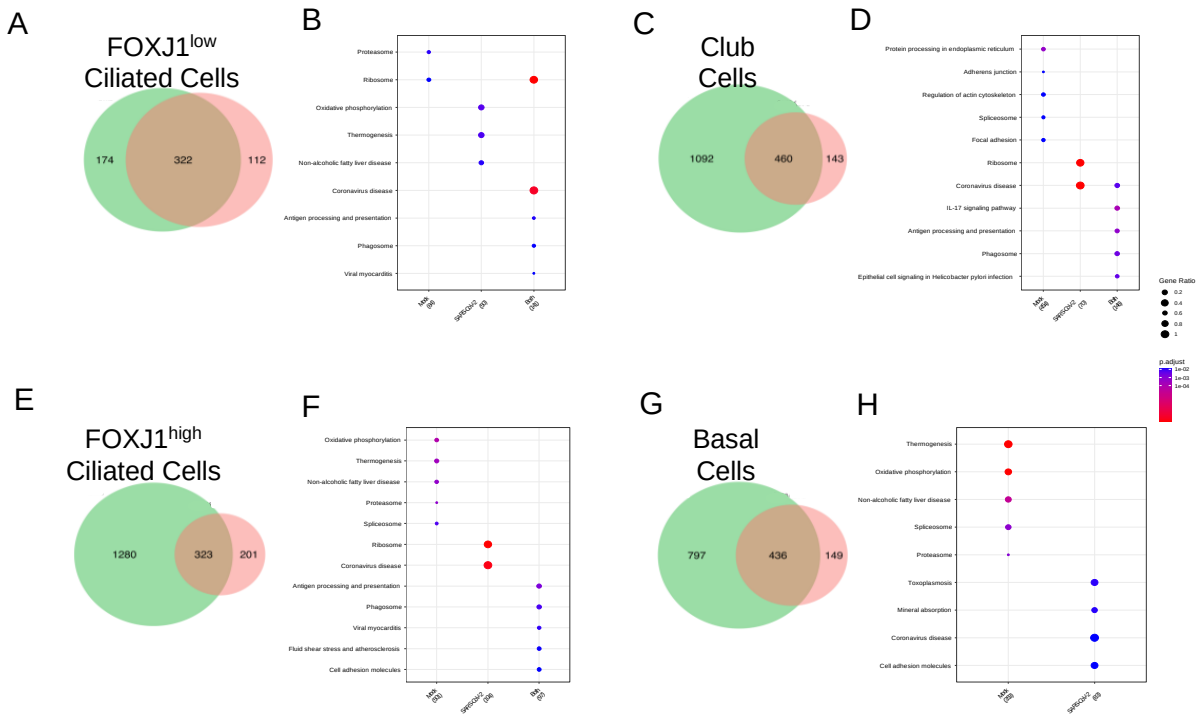

814

815 **Fig 4. Age-related differential expression analysis.** (A-H) Venn diagrams and dot plots of
816 differentially expressed genes in pediatric vs adult donors present in mock (CTRL, green) and

bioRxiv preprint doi: https://doi.org/10.1101/2024.04.02.587663; this version posted April 2, 2024. The copyright holder for this preprint (which was not certified by peer review) is the author/funder, who has granted bioRxiv a license to display the preprint in perpetuity. It is made available under aCC-BY 4.0 International license.

817 SARS-CoV-2-infected (red) samples for FOXJ1^{low} ciliated cells (A and B), club cells (C and D),

818 FOXJ1^{high} ciliated cells (E and F), and basal cells (G and H).

819

820

	Combined Senders	Combined Receivers	CTRL Senders	CTRL Receivers	SARS-CoV-2 Senders	SARS-CoV-2 Receivers	Pediatric Senders	Pediatric Receivers	Adult Senders	Adult Receivers
FOXJ1low Ciliated Cells	339	95	362	94	333	90	311	89	433	119
Club Cells	1809	1815	1881	1916	1757	1778	1627	1746	2104	2217
FOXJ1high Ciliated Cells	1695	1698	1661	1853	1653	1676	1623	1704	1821	1838
Basal Cells	2201	2016	2247	2081	2145	1981	2098	1910	2385	2175
Multiciliated Precursors	1739	1843	1890	1868	1689	1734	1730	1638	1868	2022
Ionocytes	1601	1917	1812	2041	1550	1868	1529	1831	1709	1949

821 **Table 1. Sender and receiver cell frequencies.** Frequency table of the predicted sender and

822 receiver cell communication.

823

bioRxiv preprint doi: https://doi.org/10.1101/2024.04.02.587663; this version posted April 2, 2024. The copyright holder for this preprint (which was not certified by peer review) is the author/funder, who has granted bioRxiv a license to display the preprint in perpetuity. It is made available under aCC-BY 4.0 International license.

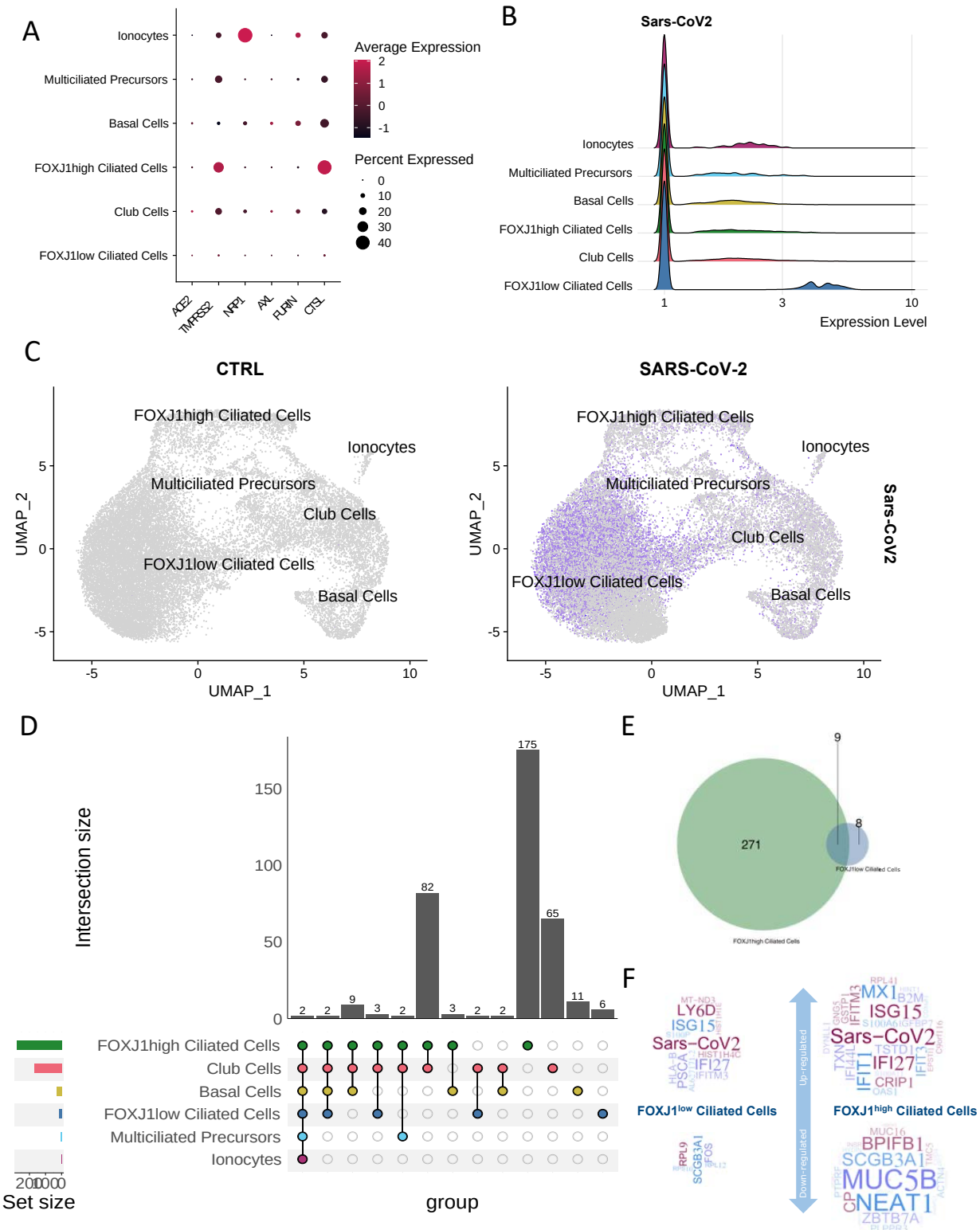

bioRxiv preprint doi: https://doi.org/10.1101/2024.04.02.587663; this version posted April 2, 2024. The copyright holder for this preprint (which was not certified by peer review) is the author/funder, who has granted bioRxiv a license to display the preprint in perpetuity. It is made available under aCC-BY 4.0 International license.

825 **Fig 5. Cell-type-specific responses to SARS-CoV-2 infection.** (A) Dotplot of scaled average
826 gene expression for indicated SARS-CoV-2 host entry factors. (B) Ridge plot of log2 normalized
827 SARS-CoV-2 expression in each cluster. (C) UMAPs of log2 normalized SARS-CoV-2
828 expression (purple) in each cell, split by treatment status. (D) An upset plot of DEGs in mock vs.
829 infected cells by cluster. (E) Venn diagram of the intersection of treatment-related DEGs
830 between ciliated cell clusters. (F) Word clouds of DEGs in ciliated cell clusters. The font size of
831 the gene names is a function of the log fold change between CTRL and SARS-CoV-2 samples.

832
833

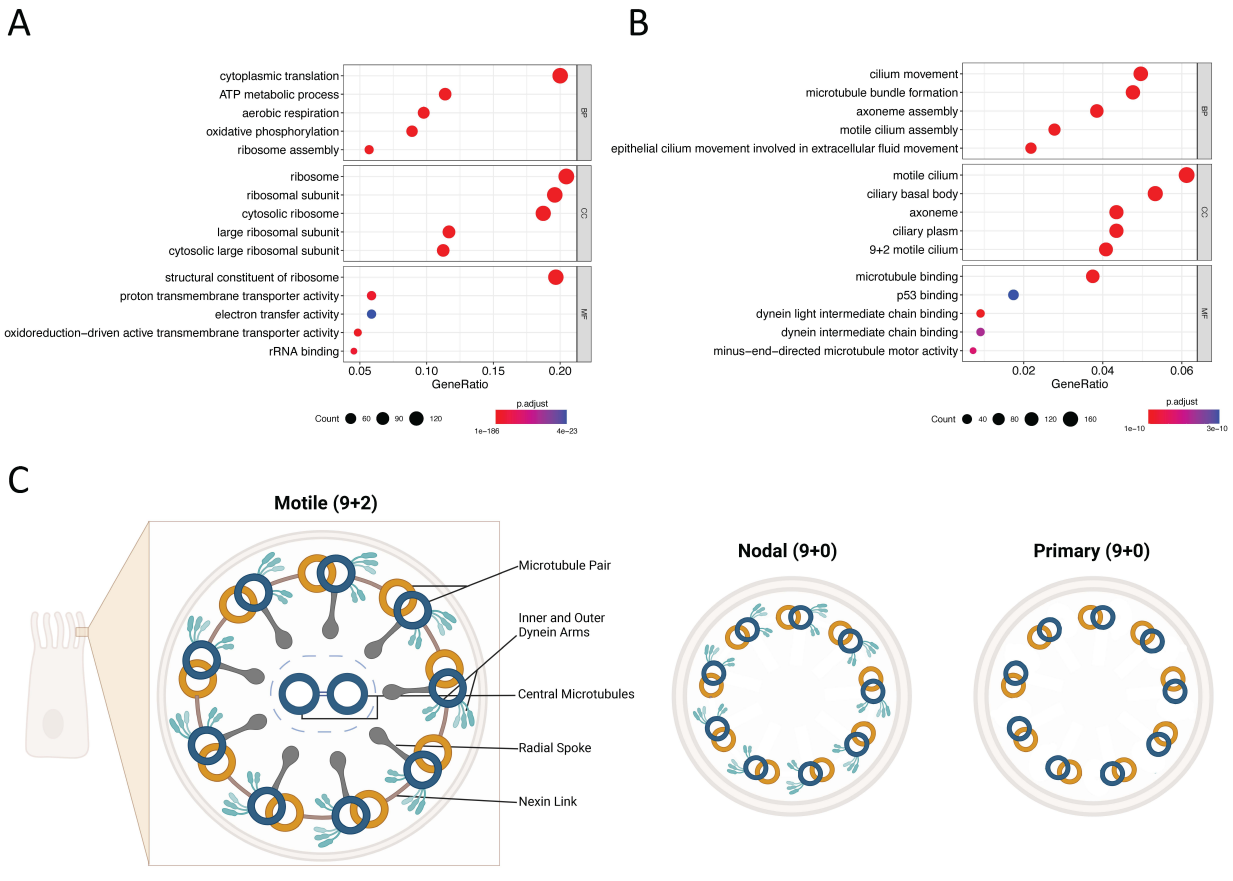

834

bioRxiv preprint doi: https://doi.org/10.1101/2024.04.02.587663; this version posted April 2, 2024. The copyright holder for this preprint (which was not certified by peer review) is the author/funder, who has granted bioRxiv a license to display the preprint in perpetuity. It is made available under aCC-BY 4.0 International license.

835 **Fig 6. Ciliated cell functional comparison.** (A and B) Dot plots of differentially enriched GO
836 terms in FOXJ1^{low} ciliated cells compared to FOXJ1^{high} ciliated cells (A) and enriched terms in
837 FOXJ1^{high} ciliated cells compared to FOXJ1^{low} ciliated cells (B). (C) Diagram of a cross-section
838 of a ciliary axoneme. Three ciliary arrangements are shown: motile cilium (9+2) on the left,
839 nodal cilium (9+0) in the center, and primary cilium (9+0) on the right.

840

bioRxiv preprint doi: https://doi.org/10.1101/2024.04.02.587663; this version posted April 2, 2024. The copyright holder for this preprint (which was not certified by peer review) is the author/funder, who has granted bioRxiv a license to display the preprint in perpetuity. It is made available under aCC-BY 4.0 International license.

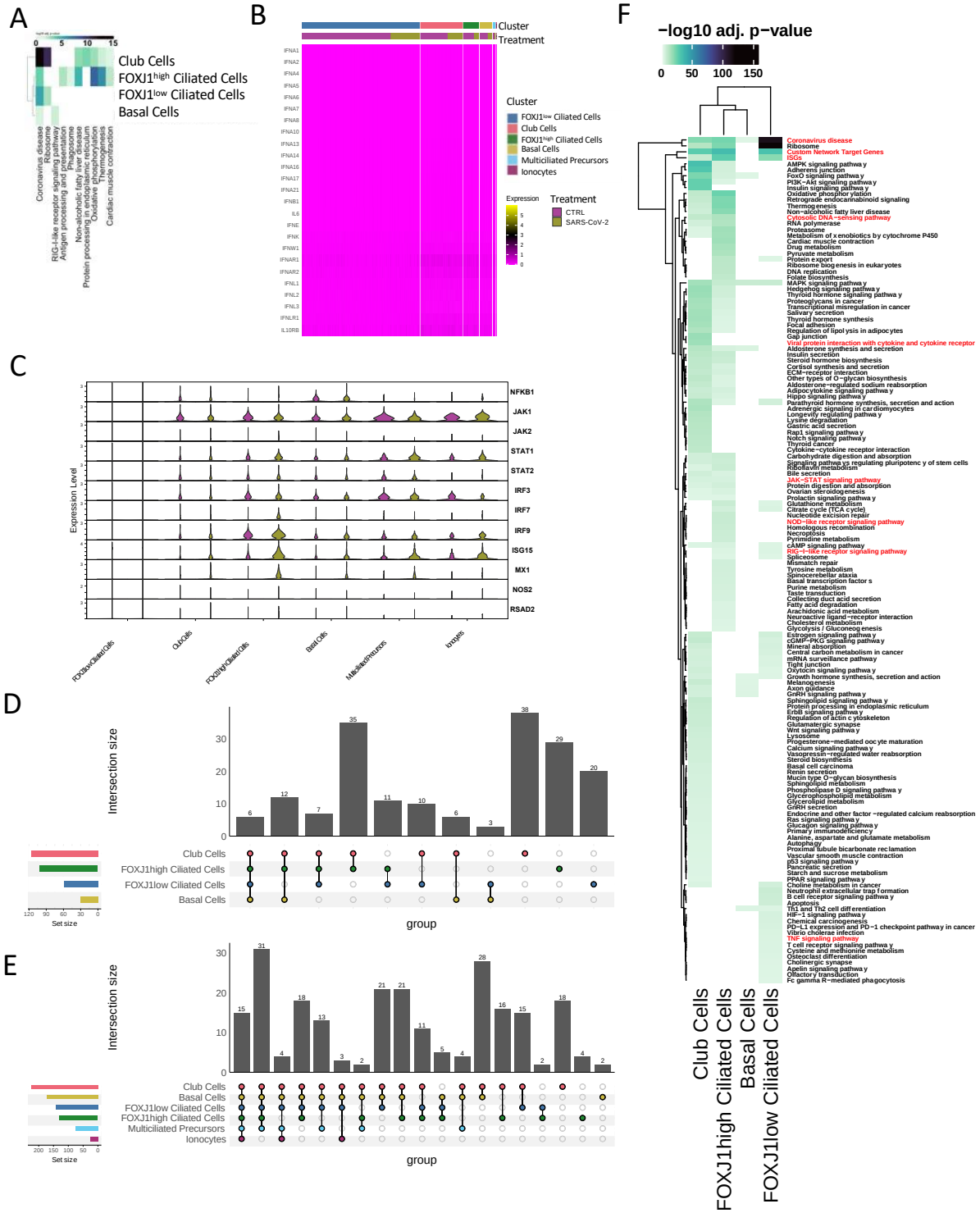

bioRxiv preprint doi: https://doi.org/10.1101/2024.04.02.587663; this version posted April 2, 2024. The copyright holder for this preprint (which was not certified by peer review) is the author/funder, who has granted bioRxiv a license to display the preprint in perpetuity. It is made available under aCC-BY 4.0 International license.

Fig 7. SARS-CoV-2 infection and cell-type-specific host responses. (A) Heatmap of -log10 adjusted p-values of differentially enriched KEGG pathways by cluster (y-axis) between mock and SARS-CoV-2-infected samples. (B) Heatmap of log2 normalized expression of indicated genes associated with a type I and type III interferon response, annotated by cluster and treatment status. (C) Violin plot of major transcription factors and intermediary genes associated with type I and III interferon responses. (D and E) An upset plot of differentially enriched AUCell scores of KEGG pathways between mock and SARS-CoV-2 treated samples (D) and pediatric vs. adult samples (E) by cluster. (F) Heatmap of -log10 adjusted p-values of significant differentially enriched AUCell scores of KEGG pathways by cluster between mock and SARS-CoV-2-infected cells. Pathways in red are typically associated with antiviral responses.

Supplementary Figures

SFig. 1. Cell cluster distribution. (A) UMAP of cells colored by sample. (B and C) UMAPs of cells are colored by cluster and split by treatment status (B) and age category (C).

SFig. 2. Cell cycle phase scoring. (A) UMAP of cells colored by cell cycle phase. (B) Stacked bar plot of cell cycle proportions by sample. (C) Stacked bar plot of cell cycle proportions by cluster. (D and F) UMAPs of cells are colored by cell cycle phase and split by age category (D) and treatment status (F). (E and G) Stacked bar plots of cells colored by cell cycle phase and

bioRxiv preprint doi: https://doi.org/10.1101/2024.04.02.587663; this version posted April 2, 2024. The copyright holder for this preprint (which was not certified by peer review) is the author/funder, who has granted bioRxiv a license to display the preprint in perpetuity. It is made available under aCC-BY 4.0 International license.

865 divided by age category (E) and treatment status (G). (H) Heatmap of integrated gene expression
866 of highly variable cell cycle markers, annotated by cluster and cell cycle phase assignment.
867
868
869 **SFig. 3. Lung epithelial cell pseudotime comparisons.** (A and B) Boxplots of the range of
870 pseudotime in each cluster, split by age category (A) and treatment status (B).
871
872
873 **SFig. 4. Cell-cell communication frequency.** (A-D) Heatmap of the frequencies of interactions
874 for each pair of potentially communicating cell types. Annotation bar plot on top ("receiving")
875 and right ("sending") is the total number of interactions per cell type subsetted by mock samples
876 (A), SARS-CoV-2-infected samples (B), pediatric samples (C), and adult samples (D).
877
878
879
880 **SFig. 5. Overview of context factorization.** "Age" and "Treatment" bar plots refer to the
881 related context loadings. The "Interactions" histogram is the frequency of individual ligand-
882 receptor pairs. "Senders" is the bar plot of loadings from sender cells. "Receivers" is the bar plot
883 of loadings from receiving cells.
884
885
886 **SFig. 6. Age-related comparative context factorization.** Boxplots of treatment (A) and age-
887 related (B) factor loadings.

bioRxiv preprint doi: https://doi.org/10.1101/2024.04.02.587663; this version posted April 2, 2024. The copyright holder for this preprint (which was not certified by peer review) is the author/funder, who has granted bioRxiv a license to display the preprint in perpetuity. It is made available under aCC-BY 4.0 International license.

SFig. 7. Heatmaps of factor loadings. (A) Sample-related factor loadings. (B and C) Sender and receiver loadings for factors 2 (B) and 10 (C).

SFig. 8. Age-related analysis of combined data. (A - C) Upset plot of differentially expressed genes in pediatric vs adult donors present in each cluster subsetted by mock-infected samples (A), SARS-CoV-2-infected samples (B), and all samples combined (C). (D) Heatmap of log10 transformed adjusted p-values of enriched KEGG pathways from differentially expressed genes in pediatric vs. adult samples. (E) Dot plot of gene ontology biological process GO terms differentially expressed genes in pediatric vs adult donors present in each cluster.

SFig. 9. SARS-CoV-2 entry factor expression. (A) Dotplot of the percentage of cells expressing the indicated SARS-CoV-2-related host entry factors split by mock-infected samples (CTRL, green) and SARS-CoV-2-infected samples (purple). (B) UMAP of log2 normalized gene expression of indicated SARS-CoV-2-related host entry factors.

SFig. 10. Exploring the pathogenic phenotype of ciliated cells. (A and B) UMAPs (A) and violin plots (B) of log2 normalized expression of canonical ciliated cell markers.

bioRxiv preprint doi: https://doi.org/10.1101/2024.04.02.587663; this version posted April 2, 2024. The copyright holder for this preprint (which was not certified by peer review) is the author/funder, who has granted bioRxiv a license to display the preprint in perpetuity. It is made available under aCC-BY 4.0 International license.

911